Supplemental Methods and Results

- Case reports
- Supplemental Figures and Figure Legends
- Supplemental tables
- Supplemental methods
- Supplemental references

Case reports

Family 1 (University of Bologna, Italy)

Proband (PT1). This 51-year-old man had poor vision since 6 years of age, when he started experiencing difficulty to see the blackboard at school. We observed this patient for the first time at 38 years of age. The neurological exam showed pale optic discs with divergent strabismus of the OS, and diffuse weak deep tendon reflexes. Lactic acid after standardized exercise was slightly elevated (15.4 mg/dl-rest; 14.5 mg/dl-rest; 30.4 mg/dl-exercise; 22 mg/dl-recovery; normal range 5.8-22 mg/dl). He underwent a first skeletal muscle biopsy, which showed only two COX-negative fibers at histoenzymatic double staining for COX/SDH. EEG recording was normal. Cerebral computerized tomography (CT) scan showed small calcifications bilaterally in the lenticular nuclei. Audiograms revealed a bilateral sensorineural hearing loss, most prominent at high frequencies (Supplemental Figure 1M). Pattern visual evoked potentials showed absent cortical responses and flash electroretinogram reduced amplitude of the retinal responses bilaterally. Brain MRI showed mild cerebellar herniation in the foramen magnum, globus pallidus calcifications, slight parietal white matter hyperintensity and chiasmal atrophy.

Kidney function was abnormal with increased creatinine and urea levels, and proteinuria. Hyperechogenic and reduced layer were described at kidney ultrasound. The EKG showed signs of left ventricular hypertrophy with evidence of increased blood pressure, and the echocardiogram was within normal limits. Urinary organic acids were normal, and so was the plasma amino acid profile, except for increased levels of taurine, glutamine, alanine and histidine.

A diagnosis of chronic kidney disease was established at 40 years of age with a kidney biopsy showing evidence of nephropathy with glomerular lesions. Histoenzymatic COX/SDH double stain revealed COX depleted areas of kidney parenchyma (Figure 2B). Kidney function

remained quite stable over the years. P31-MRS showed normal values after exercise with a slight increase of the inorganic phosphate levels at rest. A second muscle biopsy performed in 2010 showed a mitochondrial myopathy with multiple COX negative fibers (Figure 2C). We evaluated for the last time this patient when he was 50 years old. Neurological examination showed bilateral optic atrophy, absent deep tendon reflexes, mild hypopallesthesia with a positive Romberg sign. Ophthalmological evaluation demonstrated visual acuity 0.125 bilaterally, and fundus examination showed bilateral optic atrophy. OCT imaging showed diffuse RNFL loss consistent with optic atrophy and bilateral focal foveal loss of cone photoreceptor EZ (inner segment /outer segment junction), configuring a hyporeflective "cavitation lesion" as seen in other congenital disorders (for details see Discussion Section in the main text). Visual fields showed a generalized defect with central scotoma (Supplemental Figure 1N). Lactic acid evaluation confirmed normal basal values (12.5 mg/dl) and after recovery (19.4 mg/dl) with pathological increase after exercise (30.1 mg/dl) (nv 5-22 mg/dl). Creatinine level was 1.78 (nv 0.5-1.2 mg/dl), creatinine clearance 59 (nv >88), urea 58 mg/dl (nv 17-43), with increased 24 hours urinary protein levels 999 mg/dl (nv<200). CPK level was 289 U/L (nv<170). Plasma amino acid evaluation showed increased leucine levels. Audiometry confirmed the presence of sensorineural hearing loss. EEG was normal. Electromyography ruled out the presence of peripheral neuropathy. Abdominal CT scan showed liver steatosis with a focal nodule (hemangioma). Brain MR spectroscopy failed to show ventricular lactic acid accumulation. Cardiological evaluation with echocardiogram remained normal. A cycle of idebenone therapy was carried out (405 mg/day) for about five years without apparent clinical benefit.

Proband's son (PT2). This 21-year-old boy was born from a dystocic delivery with perinatal respiratory insufficiency and neonatal jaundice. He had a regular psychomotor development. He was noted to have a poor vision since seven months of age and at four years he was

diagnosed with optic atrophy. At 7 years of age, the day after a febrile illness, he was hospitalized because of a single episode characterized by hearing dysperception with sudden intolerance to noise, confusion, and psychomotor agitation. This episode lasted about 12 hours and the critical EEG recording showed focal spike-waves with parieto-occipital localization on the left hemisphere. A cerebral CT scan was judged normal. Laboratory exams performed at that time showed increased creatinine and urea levels with proteinura and increased blood pressure. A kidney biopsy showed a picture of chronic nephropathy: multifocal tubular atrophy, senescent glomeruli, interstitial fibrosis and initial vasculopathy. The residual parenchymal showed features of compensatory hypertrophy. Histoenzymatic stain showed hyper-intense SDH and reduced COX activities (Supplemental Figure 1B). Electron microscopy showed involution features of glomeruli: wrinkling ant thickening of glomerular basal membrane, mesangial matrix deposition, capillary collapse and focal podocyte foot process effacement. No electrondense deposits were observed. Many tubular epithelial cells contained numerous and abnormal mitochondria characterized by dilatation, fragmentation and loss of the cristae, and rarefaction of matrix giving them a "clear/empty" appearance (Supplemental Figure 1C, D, E, F). Apical pole maintained well-structured microvillous brush border (E). In a few tubules, scattered epithelial cells contained a normal numbers of morphologically preserved mitochondria (F). Both interstitial endothelial cells (I) and fibroblasts (J) contained abnormal mitochondria. (Supplementary Figure 1I-J). Cerebral MRI and echocardiogram were both normal. Over the time the parents noticed a slowly progressive worsening of his visual function. He also presented recurrent episodes of vomiting (about once a day) after meals associated with pallor and lethargy, from early childhood to 16 years of age.

We observed the patient for the first time at 8 years of age and neurological exam showed a pale optic disc with divergent strabismus in OD, nystagmus in both the primary position and

lateral movements of the eye, and diffuse weak deep tendon reflexes. Lactic acid after standardized exercise was abnormally elevated (11.1 mg/dl-rest; 9.9 mg/dl-rest; 33 mg/dl-exercise; 21 mg/dl-recovery; normal range 5.8-22 mg/dl). EEG was normal except for the presence of myoclonic jerks without cortical correlate. Audiogram was within normal limits. 31-P muscle spectroscopy at rest showed increased inorganic phosphate levels. Visual evoked potentials showed the absence of occipital responses bilaterally. Flash electroretinogram showed reduced amplitude of the retinal responses bilaterally.

In the following years optic atrophy and kidney insufficiency progressed. Lab exams at 17 years of age showed normal urinary organic acid except for mild increase of xantine, increase of alanine, cytosine and cysteine levels, and a picture of kidney insufficiency with pathological increase of creatinine 5.2 mg/dl (nv 0.5-1.2), urea 169 mg/dl (nv 15-50), and 24h protein levels 25 mg/dl (nv<15). The patient started dialysis and a renal transplant was finally performed at 20 years of age. Currently he is on immunosuppressive drugs (tacrolimus and micophenolate) in a well-compensated condition. Idebenone therapy was administered at 12 years of age (270 mg/day) for about one year and then withdrawn for the deterioration of the renal function.

We observed the patient for the last time at 20 years, after being stabilized for the renal transplant. Neurological examination showed bilateral optic atrophy, right exotropia, convergence defect, nystagmus, mild postural tremor at upper limbs (R>L) with parcellar myoclonic jerks and weak deep tendon reflexes. Brain MRI showed two small gliotic peritrigonal white matter lesions and chiasm atrophy. Brain MR spectroscopy did not show lactic acid in the ventricles. Electromyography ruled out a peripheral neuropathy. Lactic acid evaluation revealed a mild increase of lactic acid levels after exercise (23.4 mg/dl) with normal baseline values (6 mg/dl, nv 5-22 mg/dl). Lab exams showed normalized kidney

function (creatinine 1.17 mg/dl, nv 0.5/1.20; urea 35 mg/dl, nv 17-43 mg/dl) and normal CPK levels (37 U/L, nv <170).

Cardiological evaluation was normal. Audiometry showed a mild sensorineural impairment on the left (Supplemental Figure 1K). Ophthalmological evaluation disclosed visual acuity 0.08 in OD and 0.05 in OS, bilateral diffuse optic atrophy and OCT showed diffuse reduction of the retinal fiber layer compatible with optic atrophy, as well as a severe thinning of all macular layers, including the outer nuclear layer, due to a severe macular/cone dystrophy type phenotype, as stated in the legend of Fig. 1A (Family1-PT2). Visual fields demonstrated a central defect bilaterally (Supplemental Figure 1L).

Family 2 (Duke University, USA)

Proband (PT3). This 23-year old, Caucasian woman of Northern European descent was born at 37 4/7 weeks gestation via vaginal delivery after induction. The pregnancy was complicated by gestational diabetes and third trimester concerns for oligohydramnios and possible intrauterine growth retardation (IUGR). At birth she was 6 lbs 4 oz and 18.5 inches long. Head circumference was not noted on available birth records. In the newborn period, she required brief oxygen supplementation, and was discharged home with her family on day 2 of life.

Ophthalmological evaluation: At 18 months of age, she developed nystagmus after sequential illnesses/flu-like symptoms during the preceding month. Retrospectively, her parents recall her having more difficulty than expected with early developmental tasks with a visual component prior to 18 months old. At 2 years of age she was diagnosed with optic atrophy of unknown etiology. Periodic vision assessments demonstrated progressive worsening of visual acuity. At her first comprehensive assessment (age 17 yr, 10 months), visual acuity was 5/200 in OD and hand motions only in OS. There was a left relative afferent pupillary defect

and bilateral pendular nystagmus. Dilated fundus examination revealed diffuse optic nerve pallor bilaterally. The macular region showed blunted foveal reflexes but enhanced vitreoretinal interface reflexes, and the retinal vasculature was extremely attenuated bilaterally, with ghost vessel-like appearance (Figure 3A). There was also bilateral peripheral hypopigmentation. At her most recent comprehensive assessment (age 23 y, 6 months), a visual acuity decline to count fingers at 2.5 feet in the right eye and hand motions only in the left was observed. Pupils were bilaterally sluggish with relative afferent pupillary defect and bilateral pendular nystagmus. Dilated fundus examination was unchanged. At this last exam, dark- and light-adapted flash electroretinograms were also obtained, and showed a cone-rod (CORD) dystrophy phenotype of moderate severity in both eyes, consistent with the clinical presentation. Representative serial RNFL and macular OCT scan are illustrated in Figure 3B-C and Figure 3D-E, respectively. At the age of 17 yr 10 months, the average peripapillary RNFL thickness was ~60-65 μm in each eye (Figure 3B). At age 23 years old, there was no significant change in the extent of the RNFL loss in either eye (Figure 3C). Macular OCT, at the age of 17 yr 10 months, showed mild thinning of all retinal layers and marked loss of the macular EZ (Figure 3D, red arrows) with foveal sparing and presence of subfoveal hyperreflectivity at the EZ/RPE interface (Figure 3D, white arrow). Follow-up evaluation at age 23 years showed significant increase in the thinning of all retinal layers, further contraction of the EZ residue (Figure 3E, red arrows) but persistent subfoveal hyper-reflectivity (Figure 3E, white arrow). Hypo-reflective cystic spaces consistent with macular edema had developed at this age as well (white asterisk).

Nephrological evaluation: She was initially evaluated by nephrology at 12 years of age after hypertension was noted during an annual well-child examination. Her initial evaluation indicated chronic renal failure stage 3-4 with an estimated GFR of 32ml/min/1.73m^2. Renal ultrasound at the time of initial nephrology assessment noted bilateral small kidneys with

increased echogenicity. At that time she was noted to be small for her age, with both height and weight at <5th percentile. Growth hormone therapy was used between 12 and 15 years of age- during which she progressed to the 25th percentile for both height and weight. By age 16, she had progressed to stage-5 chronic kidney disease / end stage renal disease (ESRD). She received a living donor transplant from her mother at 16 years of age.

Audiologic evaluation: At age 18 years she developed sudden left-sided tinnitus and fluctuating sensorineural hearing loss one day after a gynecologic procedure requiring medication for sedation. She had no resolution following an initial oral steroid course. An MRI of the brain and internal auditory canals was unremarkable. Three months later she developed sudden right-sided hearing loss. Repeat assessment 4 months after initial hearing loss onset noted symmetrical normal hearing. Periodic and intermittent tinnitus and hearing loss have been treated with prednisone, most recently at age 23 years. She has a left hearing aid, but uses it only intermittently, as she reports often hearing adequately without it.

Other findings: An echocardiogram at age 15 years demonstrated trace mitral valve insufficiency, mild aortic valve insufficiency, and normal biventricular systolic function. At age 17 she began to experience chronic frontal headaches (2-3 times weekly) that are often triggered by light. After an unrevealing ophthalmology assessment, it was suggested she might have an atypical migraine or other type of chronic headache. Speech is slightly slow but with no dysarthria. She does not have a positive finger-nose test or dysdiadokinesis. Gait is normal given the visual impairment, but she does have mild difficulty with a tandem gait. Romberg is negative. Deep tendon reflexes and muscle power are normal. There have never been cognitive concerns. She is a high performing student. Family history includes three unaffected full siblings (two older, one younger).

Family 3 (University of Bologna, Italy)

Proband (PT4). A 76-year-old male was referred for a bilateral visual loss since the age of 20. Visual acuity was 4/10 in OD and 3/10 in OS with no color perception at HRR test. Fundus examination revealed temporal optic disc pallor and macular pucker in right eye and pigment epithelium dystrophy in left eye. His past medical history was remarkable for a cerebral stroke and cardiac bypass.

Family 4 (University of Bologna, Italy)

Proband (PT5). This 57-year-old male suffered a progressive visual loss since early infancy. His visual acuity was 1/30 in OD and 1/20 in OS with no color perception at HRR test. Fundus examination revealed diffuse optic disc pallor and macular dystrophy with evidence of a foveal cavitation lesion at OCT (Figure 2A, Family 4-PT5).

Proband's son (PT6). The 22-year-old male son of the proband had a poor visual function since childhood. He was corrected for myopia since 6 years of age. His visual acuity was 1/10 in OD and 2/10 in OS. HRR test was 0/6. Optic disc pallor and macular dystrophy were evident, with initial stages of foveal cavitation (Figure 2A, Family 4-PT6). Blood exams showed normal creatinine and glomerular filtration velocity values, however it was evident an increase of urea (62 mg/dL, nv 5-50 mg/dL), calcium (10.7 mg/dL, nv 8.1-10.4 mg/dL) and urate (8.3 mg/dL, nv 3.5-7.2 mg/dL) levels. Urinary analysis showed increase of protein levels (50 mg/dL, nv 0-10 mg/dL). Overall, a slight kidney dysfunction is apparent.

Proband's daughter (PT7). The 16-year-old daughter of the proband suffered a progressive visual loss since she was 3 years old. Her visual acuity was 2/10 in both eyes and color test HRR was 0/6. Temporal pallor of the optic disc and macular dystrophy were also present, again displaying initial stages of foveal cavitation (Figure 2A, Family 4-PT7). Blood exams

showed normal creatinine and glomerular filtration velocity values, however it was evident an increase of urea (65 mg/dL, nv 5-50 mg/dL) and urate (7.3 mg/dL, nv 3.5-7.2 mg/dL) levels. Overall, milder kidney alterations were observed.

Family 5 (Medical University Innsbruck, Austria)

Proband (PT8). As early as by the age of four, the index patient exhibited gait and stance problems. Hand coordination was found somewhat clumsy. The patient achieved standing and walking abilities only little behind normal age. The patient exhibited progressive sensory-neuronal hearing loss and retinitis pigmentosa leading to blindness and deafness in early adulthood. Ataxia interfered with the patient's inability to see and hear normally, but remained stable without major progression to date. The patient is still ambulant with little help. His SARA Scores (Scale for the Assessment and Rating of Ataxia; 2014, 2017) are 12 points and 14 points respectively. At the age of 6 years scoliosis was noted first but remained stable. Currently, at the age of 30 years, his height is 178 cm and body weight is 63 kg (BMI 19.9). The patient suffers from migraine without aura since childhood. In adolescence and adulthood migraine attacks became progressively bothersome. Frequency of migraine attacks is up to several times a month. Hypertrophic cardiomyopathy was diagnosed during childhood as well as impaired renal function, both being progressive. Cognition is moderately impaired at the age of 32 but interferes little with activities of daily life. He is still able to live a social life within his family despite progressive blindness, deafness and ataxia.
Extensive routine diagnostic work-up included muscle biopsy at the age of 13 years. Muscle biopsy of the quadriceps muscle revealed cytochrome-c-oxidase negative fibers without ragged-red-fibers. Biochemical evaluation detected reduced activity of complex I and complex III activity in the skeletal muscle. Hypertrophic cardiomyopathy was relatively stable between 2004 and 2016. Systolic ejection fraction of the left ventricle at last

echocardiography was >35%, NYHA staging was graded II in 2017. Electrocardiogram (ECG) shows signs of left ventricular hypertrophy. In 24 hours ECG there was no evidence of cardiac arrhythmia. NT-proBNP is unremarkable to date, while creatine kinase of skeletal muscle tends to outrange normal values especially after physical activity (up to >500 U/l, normal range 80-175 U/l). Serum Glucose and long-term HbA1c values remained normal since 2004. Renal function was found increasingly impaired and was staged as chronic renal failure stage III in 2017 (estimated GFR 49 ml/ min/1,73 m2). Extensive routine diagnostic work-up including systemic blood cell chemical analysis was unrevealing. There was no evidence of an involvement of other organs like liver, spleen or the hematopoietic system.

Supplemental Figures and Legends

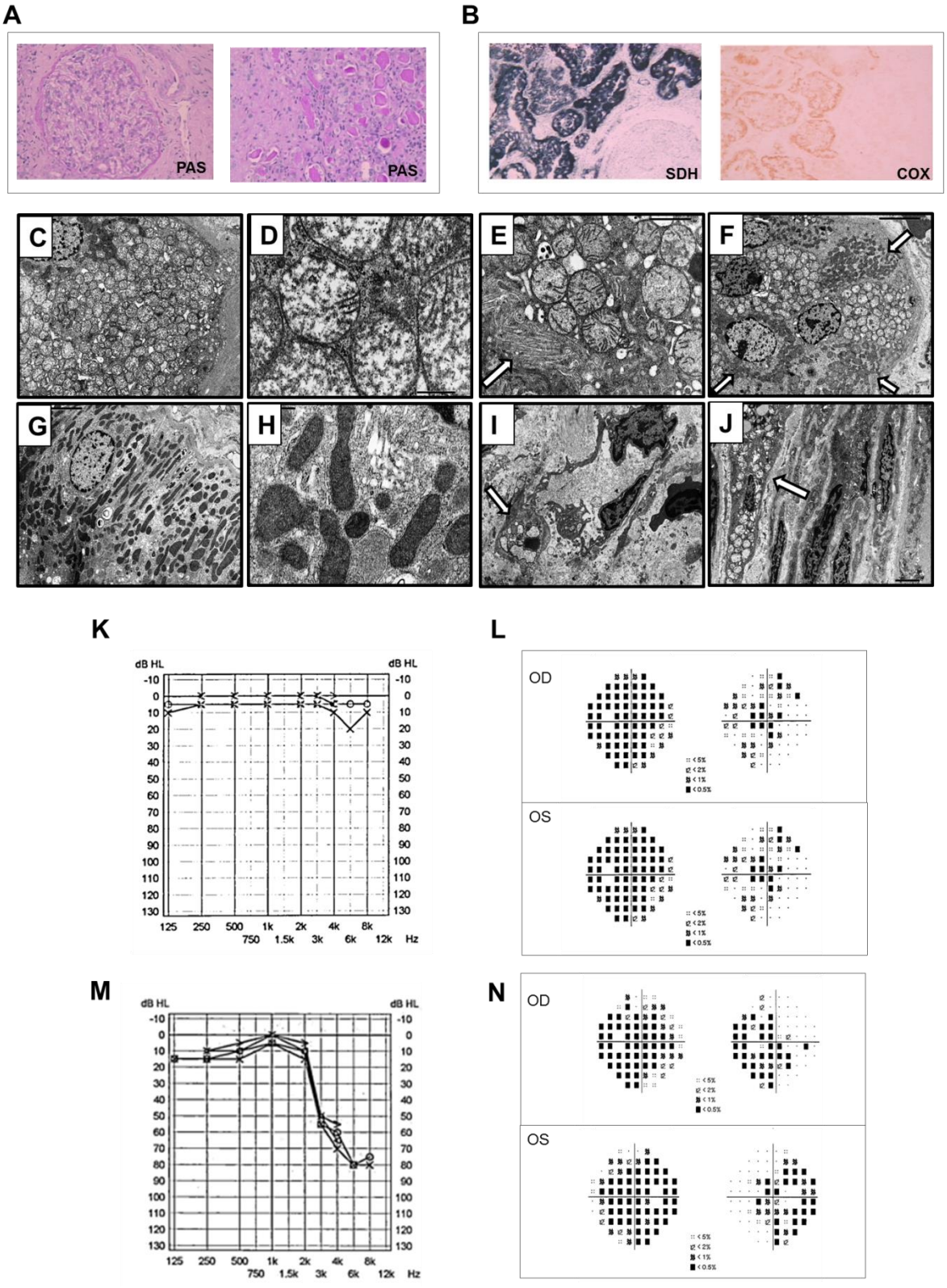

Supplemental Figure 1. Kidney characterization, audiometry and visual fields of patients carrying *SSBP1* mutations

(A) Renal histology of PT2 (R107Q II). Preserved glomerular structure and mild mesangial hypercellularity (left) secondary to chronic tubule-interstitial nephropathy and multifocal tubular atrophy containing hyaline casts and surrounded by reactive interstitial inflammation (right) (PAS stain). Residual tubules showed compensatory hypertrophy (not shown).

(B) Kidney histoenzimatic assay of PT2 (R107Q II): marked succinate dehydrogenase (SDH) activity (left) and weak Cytochrome-c-oxidase (COX) activity (right) of tubular epithelial cells.

(C-F) Renal transmission electron microscopy (EM) of PT2 (R107Q II): the majority of tubular epithelial cells contained numerous and abnormal-shaped mitochondria characterized by dilatation, loss of the cristae, and matrix rarefaction giving them a "clear/empty" appearance (C, D, E, F). Apical pole maintained well-structured microvillous brush border (E, white arrow). In a few tubules, scattered epithelial cells contained normal numbers of morphologically preserved mitochondria (F, white arrows).

(G, H) Renal EM of normal human kidney: well-oriented, oval mitochondria, in parallel distribution in the cytoplasm of tubular epithelial cells (E). Normal mitochondrial structure, with parallel and regular cristae embedded in a homogeneous dense matrix (F).

(I, J) Renal EM of PT2 (R107Q II): both interstitial endothelial cells (I, white arrow) and fibroblasts (J, white arrow) contained abnormal mitochondria, with similar features as observed in tubular epithelial cells.

Images' magnification: A 40x and 20x; B 40x; C 10000x; D 20000x; E 15000x; F 10000x; G 10000x; H 15000x; I 6000x and J 5000x.

(K) Audiometry of PT2 (R107Q II) shows a unilateral very mild loss for high frequencies indicating an initial stage of sensorineuronal hearing loss.

(L) Visual fields of PT2 (R107Q II) show a small central scotoma at pattern deviation with same more widespread losses, congruent with his childhood onset optic atrophy.

(M) Audiometry of PT1 (R107Q I) shows bilateral loss of high frequencies indicating fully expressed sensorineuronal deafness.

(N) Visual fields of PT1 (R107Q I) shows a widespread defect at pattern deviation, congruent with his severe optic atrophy.

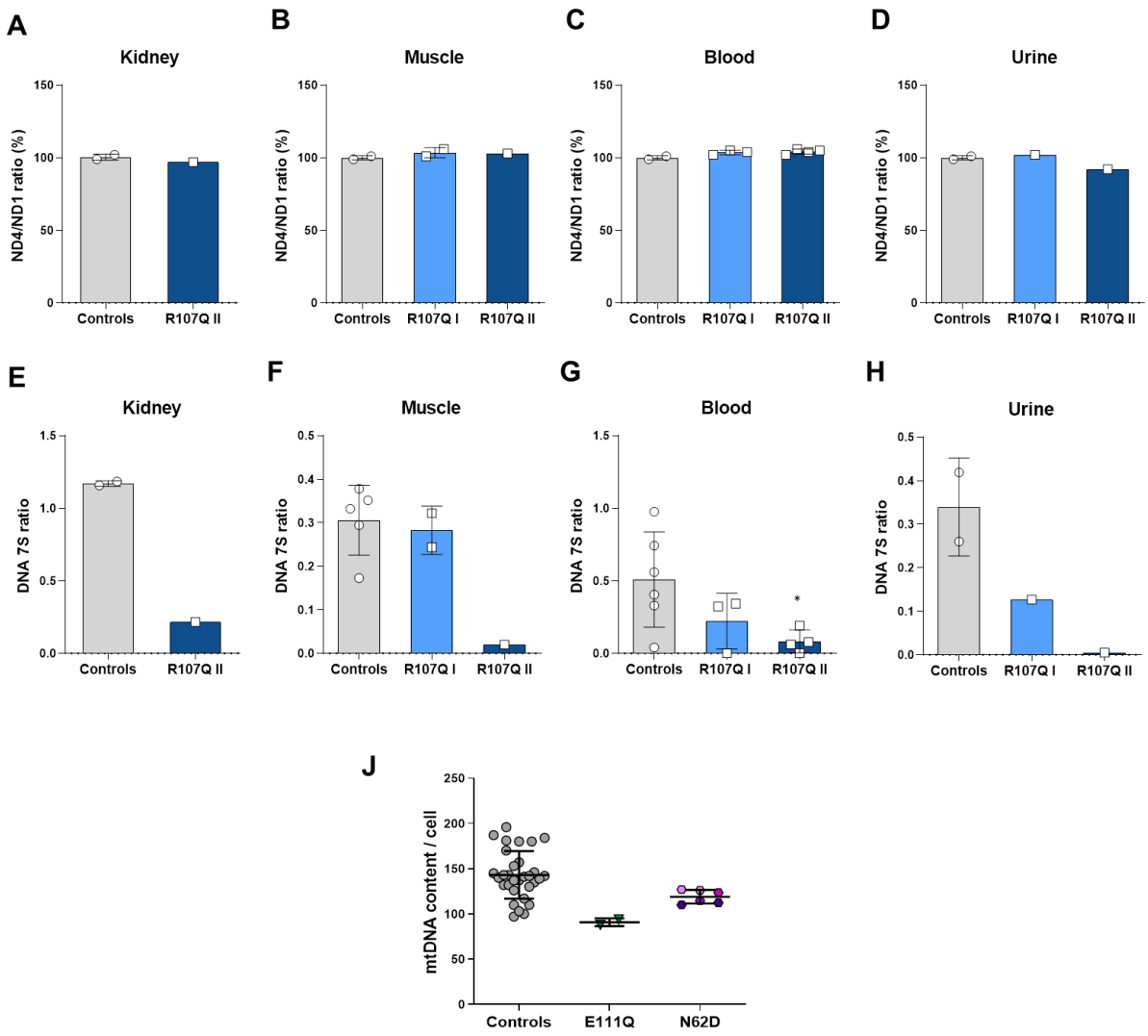

Supplemental Figure 2. Quantification of mtDNA deletions, mtDNA and 7S DNA amount on tissues

(A-D) Absolute quantification of mtDNA deletion by duplex ddPCR is expressed as percentage of ND4 (minor arc, commonly deleted) on ND1 (major arc, commonly not deleted). Data are shown as mean ± SD of 3 controls for each tissue and R107Q patients (for R107Q I, 1 kidney sample, 2 muscle, 3 blood, 1 urine sediment; for R107Q II, 1 kidney sample, 1 muscle, 1 blood, 1 urine sediment). No deletions were observed.

(E-H) The absolute quantification of mtDNA deletion and 7S DNA was carried out on kidney, muscle, blood and urine sediment from Family 1 probands (R107Q I, R107Q II). *

denotes values significantly different from the controls ($p<0.05$) of 7S DNA amount only on blood of R107Q II compared to controls, using 1-way ANOVA with Dunnett's correction.

(J) mtDNA copy number from blood samples of healthy individuals (controls) and patients from Family 3 (E111Q) and Family 4 (ND62D): PT4 (green), PT5 (dark violet), PT6 (light violet) and PT7 (pink) Data are shown as mean ± SD of 31 controls and patients (1 blood samples for each patients, analyzed in 2 experiments).

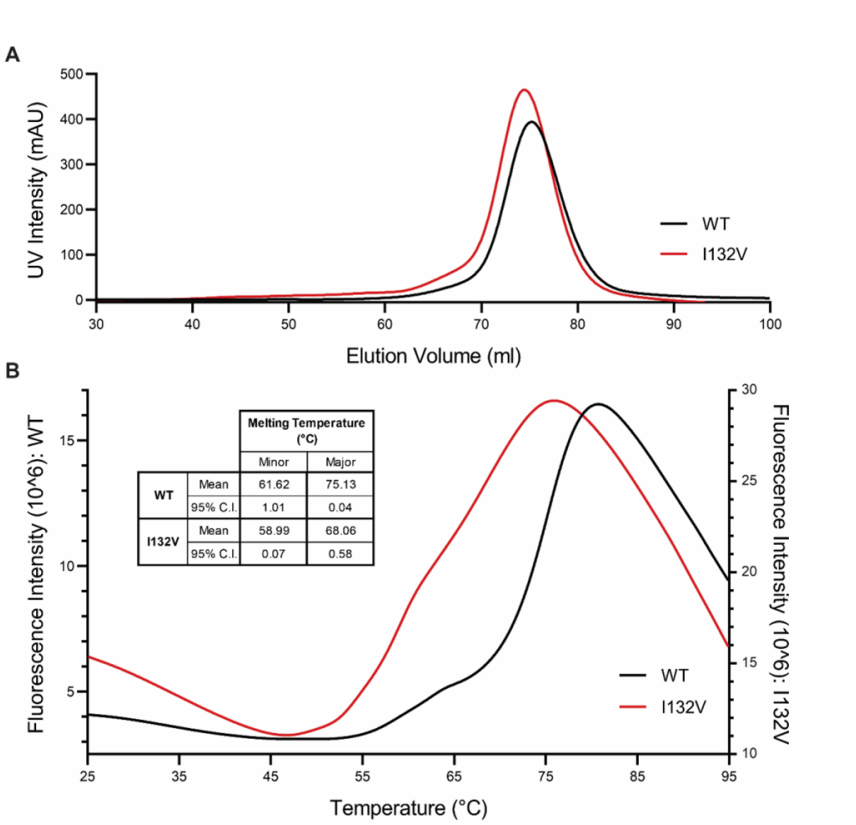

Supplemental Figure 3. *In vitro* analysis of p.I132V mutation

(A) UV intensity is plotted against elution volume for size exclusion chromatography of WT SSBP1 and p.I132V SSBP1.

(B). Thermal denaturation traces for WT and p.I132V SSBP1 are overlaid. Inset table displays average melting temperatures for minor (leftmost) and major (rightmost) melting peaks for each protein (n = 3). Differences between values for WT and p.I132VK at minor and major melting peaks are statistically significant (minor, p = 0.0178; major, p = 0.0010).

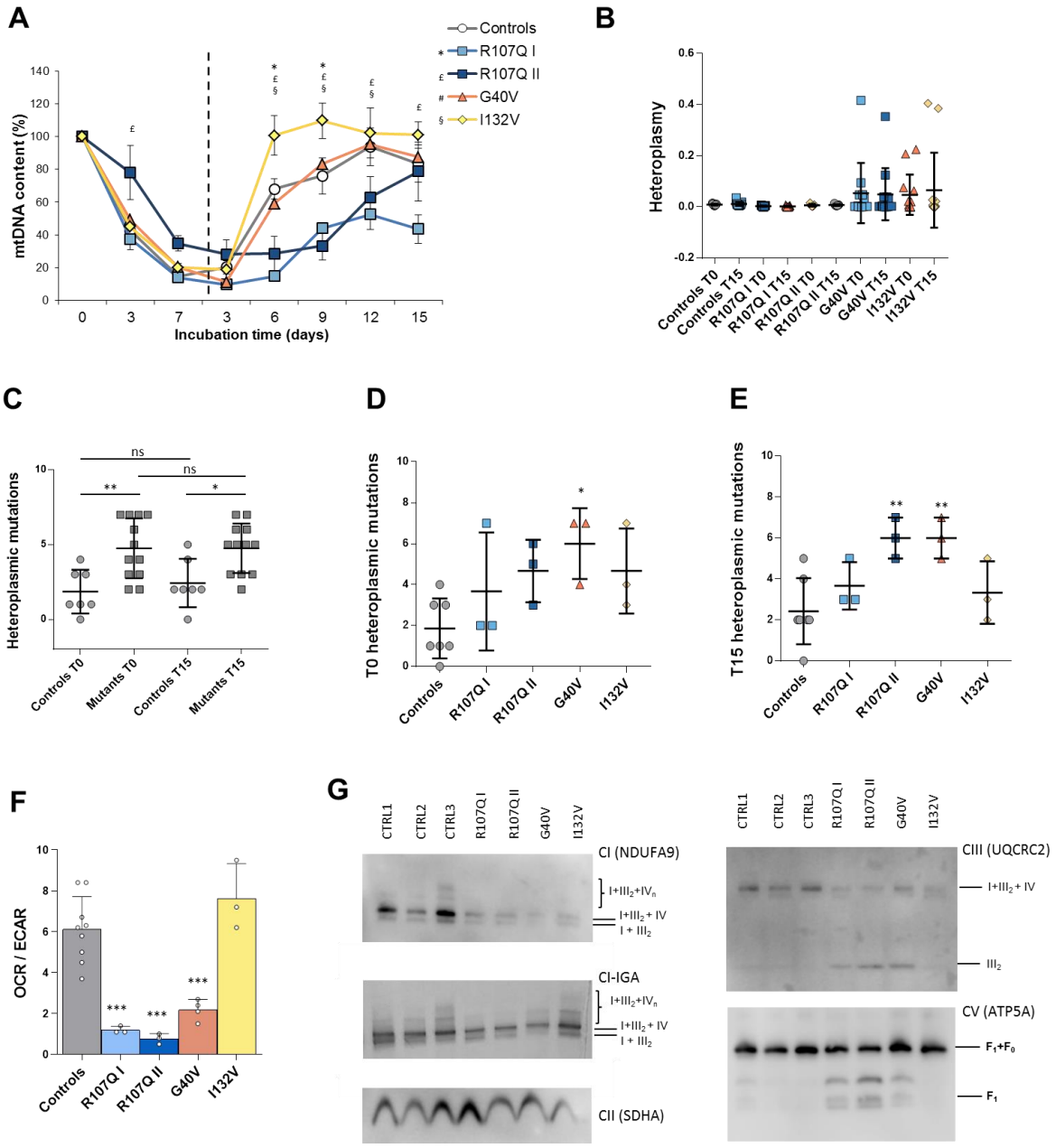

Supplemental Figure 4. Mitochondrial profile of *SSBP1* mutated fibroblasts

(A) Mitochondrial DNA repopulation after depletion by ethidium bromide in fibroblasts. mtDNA content was normalized on Day 0 before EtBr treatment and is shown as mean ± SEM of controls (n=7) and mutant cells (n=3). *,£, # and § denote values significantly different from the controls ($p<0.05$) of R107Q I, R107Q II, G40V and I132V cells,

respectively. The slowest cell lines to repopulate mtDNA content were R107Q I and R107Q II.

(B) The frequency of all variants within 90% in fibroblasts before EtBr depletion (T0) and repopulation (T15) in controls, R107Q I, R107Q II, G40V and I132V cells doesn't shown any changes between controls and mutants, and after bottle neck induced by depletion. Data are presented as scatter plot with mean ± SD.

(C-E) The number of heteroplasmic variants within 20% are presented as scatter plot with mean ± SD of aggregating cell lines (R107Q I, R107Q II, G40V and I132V) before EtBr depletion (T0) and after repopulation (T15) in C. Data of single cell lines are presented in D for T0 and in E for T15. Asterisks denote values significantly different from the controls (* $p<0.05$, ** $p<0.01$) using 1-way ANOVA with Tukey's correction. An overall increase of low heteroplasmic levels (universal heteroplasmy) was noticed in mutant fibroblasts.

(F) Analysis of the OCR/ECAR ratio under basal conditions. ECAR is an indicator of lactic acid production. The reduced OCR/ECAR ratio observed in p.R107Q and p.G40V fibroblasts suggests the occurrence of a glycolytic shift. Data are means ± SEM of control (n=7) and mutant cells (n=3). *** denotes values significantly different from controls using 1-way ANOVA with Dunnett's correction.

(G) Supercomplexes analyzed in digitonin-solubilized mitochondria by blue native (BN)-PAGE and evidenced by CI IGA and Western Blot. A reduction of supercomplexes containing CI and a partially disassembled CV are visible for p.R107Q and p.G40V cells. SDHA (CII) was used as a loading control. Supercomplexes composition and single complexes are indicated. A representative experiment out of three is shown.

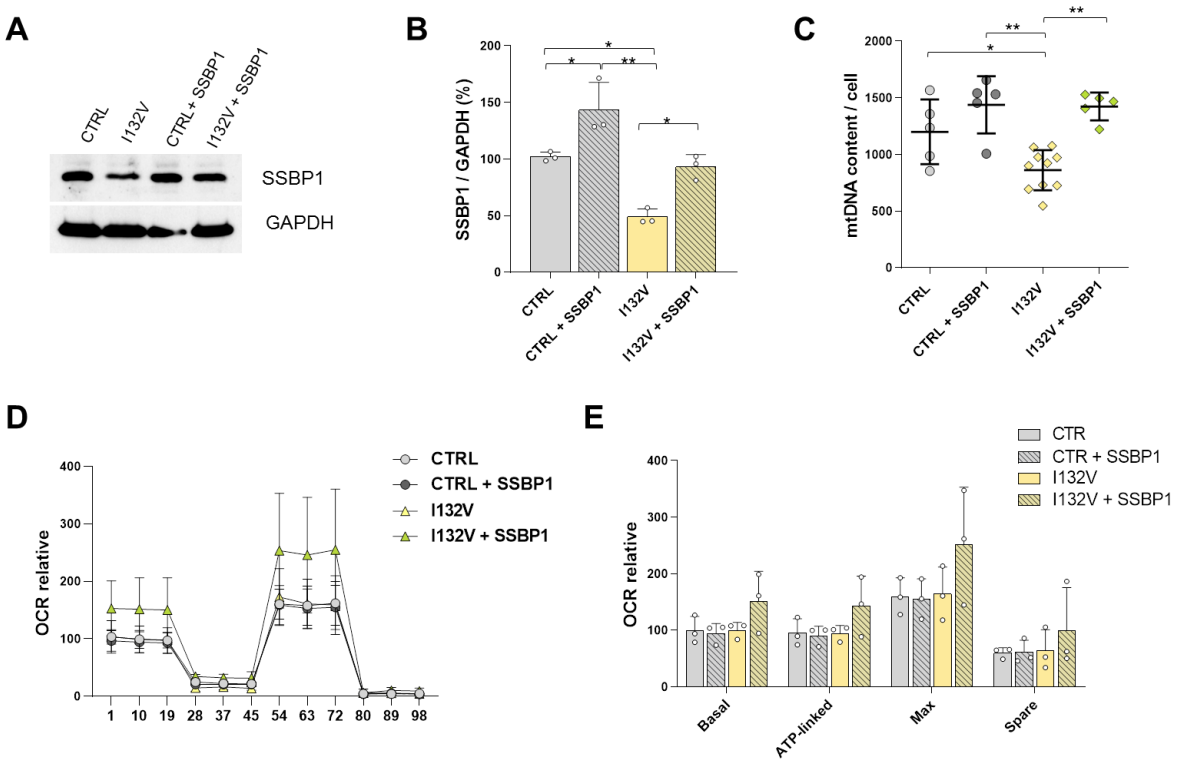

Supplemental Figure 5. Characterization of SSBP1-complemented fibroblasts

(A) Western blot analysis of SSBP1 protein levels in fibroblasts overexpressing wild-type protein. A representative blot out of three independent experiments is shown.

(**B**) Densitometric analysis of (A) shows an increase of SSBP1 amount after overexpression. All values (means ± SEM) are normalized to control cells.

(**C**) mtDNA copy number quantification reveals the rescue of depletion in the p.I132V mutant cells. Data are means ± SEM of controls (n=5), SSBP1-complemented control (n=5), p.I132V cells (n=10) and SSBP1-complemented p.I132V cells (n=5).

(**D**) OCR of fibroblasts, expressed as pmoles O2/min normalized for protein content, under basal conditions and after injection of oligomycin (O), carbonyl cyanide 4-(trifluoromethoxy) phenylhydrazone (FCCP; F), rotenone (R) and antimycin A (AA). Data are normalized for the basal respiration of the respectively un-complemented cells, and are expressed as means ± SEM of three independent experiments.

(**E**) Basal, ATP-linked, maximal respiration and spare respiratory capacity were calculated from OCR traces and are reported in the graph as means ± SEM. OCR experiments show a slight increase of respiratory capacity in SSBP1-complemented p.I132V cells.

Asterisks denote values significantly different from the controls (* $p<0.05$, ** $p<0.01$).

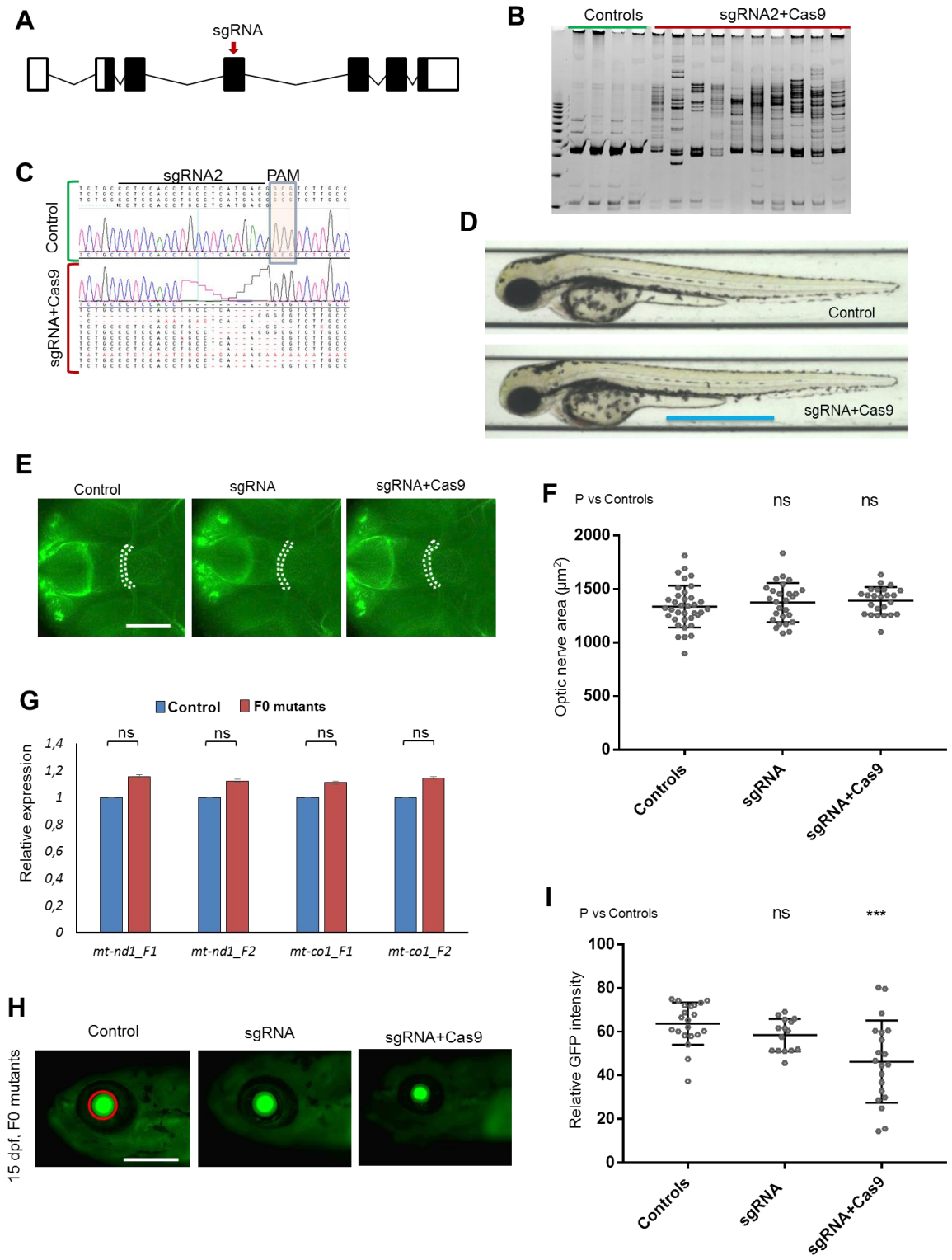
A
sgRNA
B
Controls
sgRNA2+Cas9
C
sgRNA2
PAM
Control
sgRNA+Cas9
D
Control
sgRNA+Cas9
E
Control
sgRNA
sgRNA+Cas9
F
P vs Controls
ns
ns
Optic nerve area (µm²)
2000
1500
1000
500
0
Controls
sgRNA
sgRNA+Cas9
G
Control
F0 mutants
Relative expression
1,4
1,2
1
0,8
0,6
0,4
0,2
0
ns
ns
ns
ns
mt-nd1_F1
mt-nd1_F2
mt-co1_F1
mt-co1_F2
H
Control
sgRNA
sgRNA+Cas9
15 dpf, F0 mutants
I
P vs Controls
ns
***
Relative GFP intensity
100
80
60
40
20
0
Controls
sgRNA
sgRNA+Cas9

Supplemental Figure 6. Efficient genome editing at the zebrafish *ssbp1* locus and mitochondrial depletion in *ssbp1* zebrafish models

(A) Schematic of the *Danio rerio ssbp1* ortholog (GRCz11, chr4: 4,752,622-4,756,349); white boxes show untranslated regions; black boxes show the coding regions; red arrow, sgRNA target site in exon 4.

(B) Heteroduplex analysis of F0 mutants. n=4 embryos assessed; 16 colonies/embryo. Polyacrylamide gel image shows efficient targeting in individual F0 embryos, compared to controls. Left lane, marker.

(C) Representative chromatograms from cloned PCR products flanking the *ssbp1* target site depict small insertion-deletions in the targeted region; PAM, protospacer adjacent motif.

(D) Representative live lateral images of control and *ssbp1* F0 mutant embryos at 2-days post fertilization (dpf) show no obvious morphological differences. Scale bar, 800 µm.

(E) Representative ventral images of wholemount 2-dpf embryos immunostained with acetylated tubulin antibody to mark the optic nerve. Dashed outline, region measured for quantification. Scale bar, 50µm.

(F) Quantification of the optic nerve chiasm area measured with ImageJ. ns, not significant according to an unpaired student's t-test; n=26-30/batch, total of four biological replicates gave similar results. Error bars represent standard deviation (SD) of the mean.

(G) Relative expression of mitochondrial markers determined by qRT-PCR from F0 mutants vs controls, and normalized to *b-actin*; the number of mitochondria in F0 mutants at 2 dpf were not significantly (ns) different from controls according to an unpaired student's t-test. F1 and F2 denote different primer pairs for each gene. Error bars represent SEM.

(H) Representative live lateral images of *Tg(XlEef1a1:mlsEGFP)* larvae at 15 dpf. Scale bar, 50µm.

(I) Quantification of GFP intensity in *Tg(XlEef1a1:mlsEGFP)* larvae acquired at 15 dpf (lens area circled in red, panel H). F0 mutants display significantly reduced GFP intensity compared to controls or sgRNA alone. N=15-30 embryos/batch. ***$p \leq 0.001$ according to an ANOVA with Tukey's correction test; ns, not significant. Error bars represent SD.

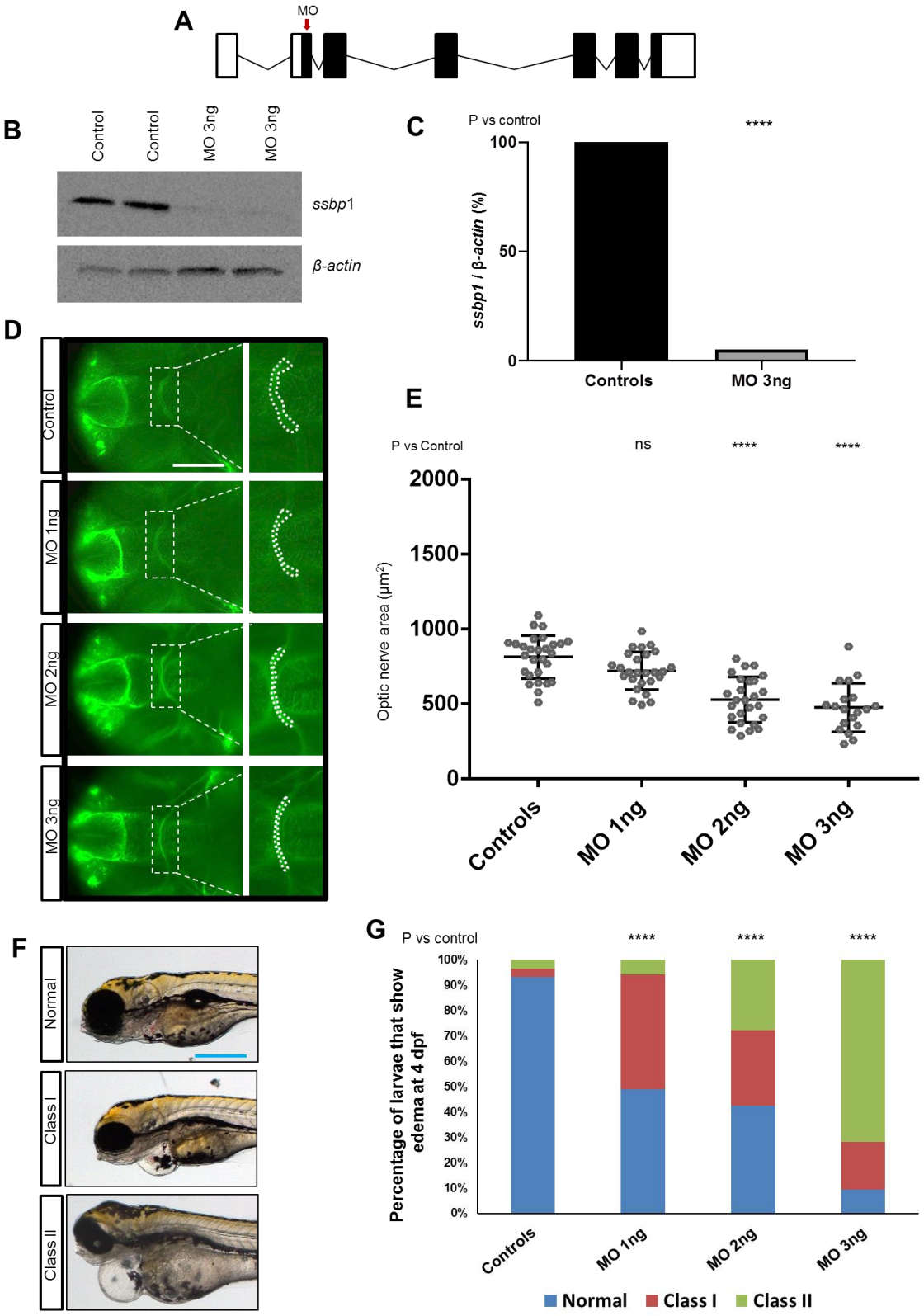
A
MO
B
Control
Control
MO 3ng
MO 3ng
ssbp1
β-actin
C
P vs control
****
100
50
0
ssbp1 / β-actin (%)
Controls
MO 3ng
D
Control
MO 1ng
MO 2ng
MO 3ng
E
P vs Control
ns
****
****
2000
1500
1000
500
0
Optic nerve area (µm²)
Controls
MO 1ng
MO 2ng
MO 3ng
F
Normal
Class I
Class II
G
P vs control
****
****
****
100%
90%
80%
70%
60%
50%
40%
30%
20%
10%
0%
Percentage of larvae that show edema at 4 dpf
Controls
MO 1ng
MO 2ng
MO 3ng
Normal
Class I
Class II

Supplemental Figure 7. *ssbp1* morpholino induces efficient suppression of *D. rerio* transcript enabling *in vivo* complementation experiments.

(A) Schematic of the *Danio rerio ssbp1* locus; white boxes, untranslated regions; black boxes, coding regions. Translation blocking (tb) morpholino (MO; red arrow) targets the initiation ATG in exon 1.

(B) Immunoblot showing efficient *ssbp1* translation blocking in morphants. Total protein was extracted from pools of whole embryos (n=25) at 2 days post-fertilization (dpf). Experiments were performed on biological duplicates (control or 3 ng *ssbp1* MO) and SSBP1 protein was detected at the expected size (17 kDa). β-actin (42 kDa) was used as a loading control.

(C) Densitometry analysis of SSBP1 immunoblot signal normalized to β-actin (panel B) shows >95% reduction in embryos injected with 3 ng *ssbp1* MO. **** denotes $p<0.0001$ using student's 1-tailed t test.

(D) Representative ventral images of whole mount 2 dpf embryos immunostained with acetylated tubulin antibody to mark the optic nerve. Dashed white box indicates magnified region in the inset at left; Dashed outline, region measured for quantification of optic chiasm area. Scale bar, 50μm.

(E) Quantification of optic nerve chiasm area in the context of increasing doses of tb MO. N=30-35/batch, total of four biological replicates. Error bars represent SD of the mean.

(F) Representative live lateral views of *ssbp1* morphant larvae at 4 dpf display edema phenotypes suggestive of renal filtration defects. Class I, pericardial edema; Class II, pericardial edema and periorbital or yolk sac edema. Scale bar, 50 μm.

(G) Qualitative scoring of edema phenotypes in *ssbp1* morphants at 4 dpf injected with increasing doses of tb MO (see panel F for scoring criteria).

For panels E, and G, ****$p<0.0001$; *$p\leq0.05$ according to an ANOVA with Tukey's correction test. Error bars represent SD of the mean.

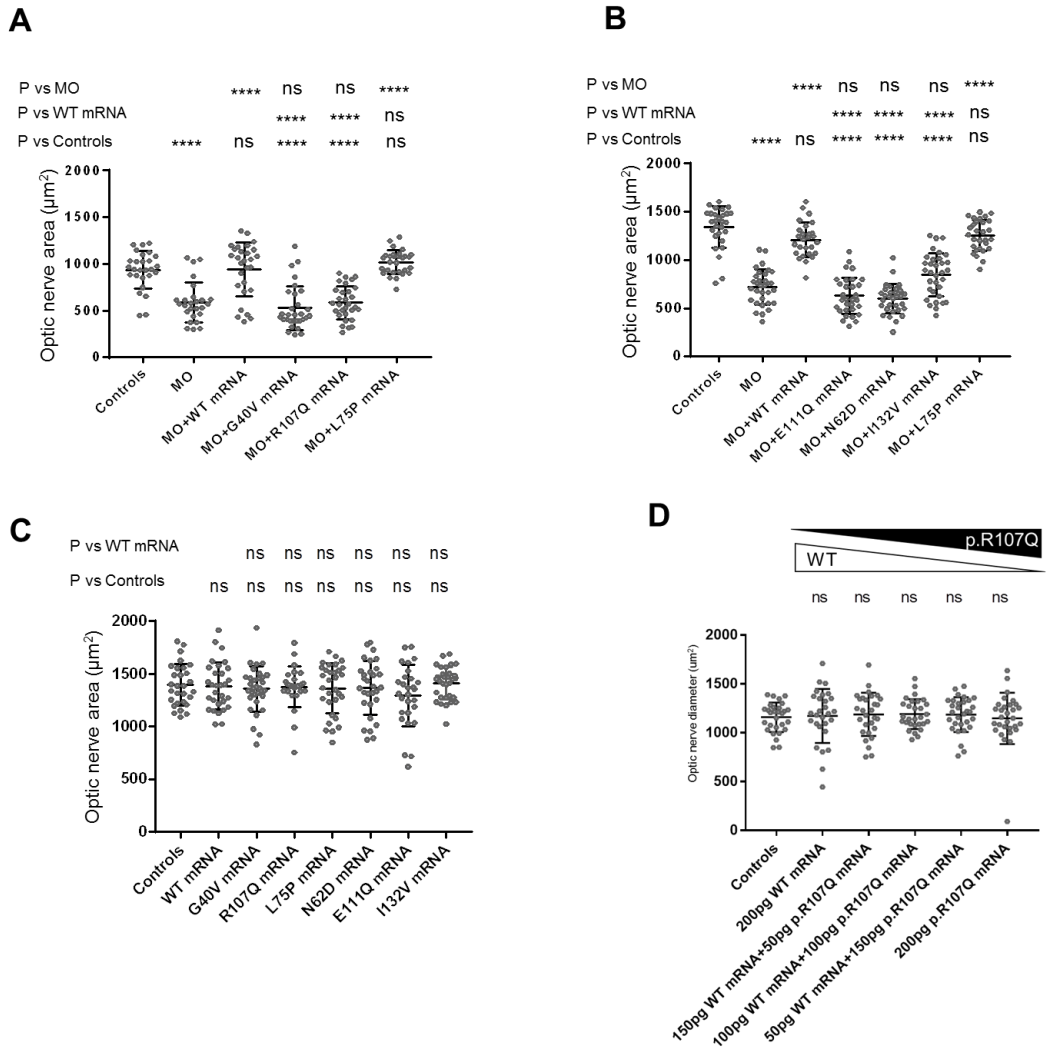

Supplemental Figure 8. Dot plots showing *ssbp1 in vivo* complementation experiments and ectopic expression of human *SSBP1* mRNA.

(A) Quantification of the optic nerve chiasm area in 2 day post-fertilization (dpf) zebrafish embryos for experiments testing MO plus mRNAs harboring p.G40V, p.R107Q and p.L75P. n=26-35 embryos/batch; three biological replicates.

(B) Quantification of the optic nerve chiasm area in 2 dpf embryos for experiments testing MO plus mRNAs harboring p.E111Q, p.N62D, p.I132V and p.L75P. n=26-35 embryos/batch; three biological replicates.

(C) Quantification of the optic nerve chiasm area in 2 dpf embryos injected with human *SSBP1* mRNA. n=26-35 embryos/batch, three biological replicates gave similar results. **(B)** To test to for dominant negative effects, we co-injected WT and p.R107Q encoding human *SSBP1* mRNAs. Quantification of the optic nerve chiasm area in 2 dpf zebrafish embryos shows no detectable phenotype across a titration curve; n=25-35 embryos/batch. See Figure 7 A,B for depiction of measurement parameters. For panels A-D, ****$p<0.0001$; ** $p\leq0.01$; p*$p\leq0.05$ according to an ANOVA with Tukey's multiple comparison test; ns, not significant; error bars represent SD of the mean for all panels.

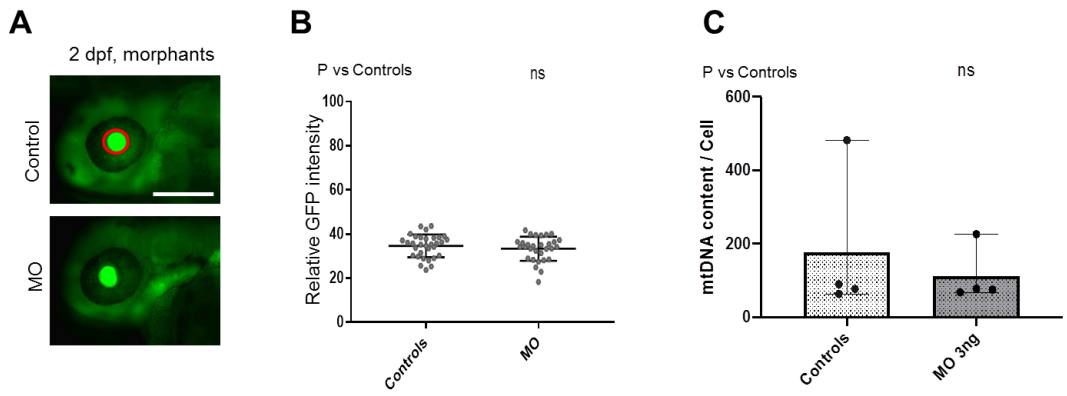

Supplemental Figure 9. *ssbp1* morphants do not display detectable differences in mitochondrial quantity or mtDNA content compared to controls at 2 days post-fertilization.

(A) Representative live lateral images of Tg(XlEef1a1:mlsEGFP) embryos acquired at 2 dpf. Scale bar, 50µm

(B) Quantification of GFP intensity in Tg(XlEef1a1:mlsEGFP) embryos at 2 dpf from a defined region in the lens (circled in red, panel C). Morphants display no detectable differences in GFP intensity versus controls. ns, not significant; n=26-30 embryos/batch.

(C) Quantification of mtDNA content in controls and *ssbp1* morphants using qPCR (2 dpf embryo pools of 30 embryos each); *mt-nd1* was the mtDNA marker and was normalized to *polg1* as a reference for nuclear genomic DNA. Experiments were performed in biological quadruplicate, with triplicate wells in each. ns, not significant. Error bars represent standard error of the mean. No differences were observed in B and C using a 2-tailed student's t-test.

Supplemental Tables

Family	Sample	Mean Coverage	% bases >20X
1	I:2	148.90	96
	I:1	134.22	95
	II:1	121.73	95
2	II:1	71.01	82
	I:1	91.80	87
	I:2	69.86	82
5	II:2	161.22	99.02

Supplemental Table 1. NGS statistics. Mean coverage and percentage of bases covered > 20X are indicated for each WES experiment.

Family	Chr	Position	Ref	Alt	Gene	MOI	cDNA/Protein	gnomAD frequency	CADD Phred	phyloP100way vertebrate
1	7	141445301	G	A	SSBP1	De novo	NM_003143.2:c.320C>A;p.Arg107Gln	NA	24.3	8.5
	10	81841422	A	-	TMEM254	De novo	NM_001270371:c.114delA;p.Ser38fs	0.007561	NA	NA
	12	100723037	C	T	SCYL2	De novo	NM_017988:c.1701C>T;p.Ala567Ala	0.00002786	8.4	NA
2	7	141443394	G	T	SSBP1	De Novo	NM_003143.2:c.119G>T;p.Gly40Val	NA	29.4	8.9
	1	52821497	T	C	CC2D1B	ARCH (paternal)	NM_032449.2:c.2092A>G;p.Ser698Gly	0.00001591	27.1	4.6
	1	52821932	G	C	CC2D1B	ARCH (maternal)	NM_032449.2:c.1998C>G;p.Ile666Met	0.00000376	22.9	1.5
	11	118344671	C	T	KMT2A	ARCH (paternal)	NM_005933.3:c.2797C>T;p.Arg933Trp	0.00003184	27.6	4.4
	11	118373914	G	A	KMT2A	ARCH (maternal)	NM_005933.3:c.7298G>A;p.Cys2433Tyr	0.00003191	16.3	0.5
	10	135012426	G	A	KNDC1	ARCH (paternal)	NM_152643.6:c.2414G>A;p.Gly805Glu	0.000629	2.4	-2
	10	135025199	G	T	KNDC1	ARCH (maternal)	NM_152643.6:c.4073G>T;p.Gly1358Val	0.001946	20.4	3.1
3	7	141445312	G	C	SSBP1	ND	NM_003143.2:c.331G>C;p.Glu111Gln	NA	25.4	8.5
4	7	141443459	A	G	SSBP1	AD	NM_003143.2:c.184A>G;p.Asn62Asp	NA	23.1	8.3
5	7	141445375	A	G	SSBP1	ARH	NM_003143.2:c.394A>G;p.Ile132Val	0.00000813	21.8	6.2

Supplemental Table 2. NGS variants. Candidate variants identified through WES or targeted gene panel are listed. Genomic, cDNA and protein positions, reference and alternative alleles, affected gene, inheritance, allele frequency, CADD Phred and PhyloP100way scores (https://sites.google.com/site/jpopgen/dbNSFP) are reported for each variant.

Homozygosity assesment of I132V			
n	UCSC position	Size (Mb)	number of SNVs
1	chr1:236384278-236718560	0,33	43
2	chr12:133104461-133796032	0,69	45
3	chr17:7226957-7477937	0,25	44
4	chr19:40883844-41928723	1,04	65
5	chr3:193334991-194061905	0,73	10
6	chr3:196650187-197581146	0,93	30
7	chr7:136587843-139653195	3,07	48
8	chr8:144944161-145004545	0,06	39

Supplemental Table 3. Homozygosity assesment of I132V. Size of largest homozygous region (3 Mb) indicates that parental consanguinity is unlikely..

Variant	Vipur	Ess.	Interpretation	Annotation
Gly40Val	0.784	0.224	unfavorable backbone conformation	ssDNA binding site
Glu111Gln	0.661	-0.056	unfavorable backbone conformation	tetramer interface
Asn62Asp	0.310	-0.269		dimer interface
Ile132Val	0.169	-0.381		
Arg107Gln	0.099	-0.427		tetramer and dimer interfaces

Supplemental Table 4. Structural and functional effect of *SSBP1* variants. *In silico* prediction scores obtained through VIPUR pipeline are reported for each variant, along with the corresponding interpretation and functional annotations.

Variant	Allele number
M1?	**14**
R3*	**1**
E27*	**1**
R66*	**4**
R107*	**2**
E146*	**1**
E148*	**1**

Supplemental Table 5. Start-loss and nonsense SSBP1 ultra-rare variants and alleles in gnomAD database

Supplemental Methods

Whole Exome Sequencing and Targeted *SSBP1* Next Generation Sequencing

Family 1

Genomic DNA purified from whole peripheral blood samples of three individuals (I:1, I:2, II:1) was enriched for whole exome sequences through Roche-Nimblegen SeqCap EZ Exome v3 kit (II:1) or BGI Exome kit (I:1 and I:2) and sequenced as 100 bp paired-end reads on Illumina HiScan SQ/HiSeq2000 systems. Generated reads were checked for quality with FastQC (http://www.bioinformatics.babraham.ac.uk/ publications.html) and aligned with BWA to the UCSC reference genome hg19. Aligned reads were treated for local realignment and base quality score recalibration with GATK and for duplicate removal with PicardTools (http://picartools.sourceforge.net). Alignment statistics were collected with SAMtools and GATK. Variant calling and filtering by quality were performed by GATK. Variants passing quality filters were annotated against Ensembl (http://www.ensembl.org/). In the three WES analysis a mean coverage > 120X was obtained and 95-96% of bases were covered > 20X (Supplemental Table 1). A *de novo* autosomal origin of a causative heterozygous variant was assumed based on pedigree where the disease appears in proband (II:1) born to healthy parents (I:1 and I:2) and is then transmitted in an apparently dominant fashion to his son (III:1) (Figure 1). We used the *de novo* variant detection tool Platypus to identify *de novo* variants. We prioritized coding or splice-site disrupting variants that were novel with respect to public population variant databases and predicted to alter the protein product. Following this prioritization, among the three candidate variants identified (Supplemental Table 2) the novel missense change NM_003143.2:c.320C>A;p.Arg107Gln in *SSBP1* emerged as the most prominent candidate. Sanger sequencing confirmed that this variant arose *de novo* and demonstrated that it was transmitted to the proband's son (III:1) (Figure 1).

Family 2

DNA was extracted from peripheral blood samples of the whole trio and exome sequencing was performed through the 65-Mb Illumina TruSeq Exome Enrichment Kit and run on the Illumina HiSeq 2000 platform at the Genomic Analysis Facility in the Center for Human Genome Variation, Duke University. Reads were aligned against the 1000 genomes b37 build (no decoys) through BWA-MEM from the GATK resource bundle. After alignment, soft-clipping of reads and duplicate read marking were performed using Picard followed by local re-alignment around indels with GATK IndelRealigner. Variant calling was done by GATK HaplotypeCaller on a per-sample basis, considering further only variants with a base quality of at least 30. Further filtering was done according to GATK best practices recommendations. Basic sequencing statistics are reported in Supplemental Table 1. The resulting VCFs were then uploaded to Sapientia (www.sapientia.co.uk) for annotation and causal variant prioritization. Variants were annotated using Ensembl Variant Effect Predictor (VEP) and scored for disease causality using Exomiser. Four different inheritance models were considered in each trio: *De Novo* occurrence, Autosomal Recessive Homozygous (ARH), Autosomal Recessive Compound Heterozygous (ARCH) and X-Linked Recessive (XLR). DeNovoGear was used for joint analysis of samples within a trio to detect *de novo* alterations. Variants with qualifying genotypes under each inheritance model were ranked using the Exomiser combined score and evaluated for rarity (MAF in ExAC and UK10K), pathogenicity (Polyphen2 and SIFT scores), genic intolerance to functional variation (RVIS and pLI scores) and biological relevance in the context of the proband's phenotype (Phenotype Consensus Analysis, PCAN, and literature search). Supplemental Table 2 lists the annotated variants identified under different inheritance models in this trio. The top ranked variant was a de novo missense change NM_003143.2:c.119G>T;p.Gly40Val in *SSBP1*, not present in the general population, predicted to be damaging and showing some biological

relevance based on PCAN analysis. Three additional genes were identified as potential recessive candidates, carrying compound heterozygous variants. Sanger sequencing confirmed *SSBP1* variant in the proband II:1and identified only wild-type alleles in the parents (I:1 and I:2) (Figure 1).

Family 3 and Family 4

A total of 135 patients with optic atrophy and mutation-negative after analysis of *OPA1* underwent *SSBP1* genetic screening of genes implicated in optic atrophy. SSBP1 was either analysed by Sanger sequencing (47 patients) or was added to a optic atrophy diagnostic panel including 35 genes (88 patients). The panel library was generated using an enzymatic fragmentation and capture approach (Nextera Rapid Capture Custom Enrichment, Illumina), and sequenced as 2x150 bp paired-end reads on Illumina MiSeq instrument. Reads were aligned to the UCSC reference genome hg19 using BWA. PCR duplicate reads were removed with the PicardTools MarkDuplicates utility, then reads were treated for local realignment and base quality score recalibration with GATK. Variant calling and filtering by quality were performed by GATK. Variants passing quality filters were annotated against RefSeq with ANNOVAR. Only rare variants (MAF<0.01 in ExAC and never seen in the homozygous state), predicted to affect the protein function, i.e. nonsynonymous, nonsense, splicing and small indels, were retained. In two patients, heterozygous missense variants in SSBP1 were found, NM_003143.2:c.331G>C;p.Glu111Gln (Family 3) and NM_003143.2:c.184A>G;p.Asn62Asp (Family 4) (Supplemental Table 2). Both variants were confirmed by Sanger sequencing. In Family 4, the variant segregated in both affected offspring of the patient analysed by the NGS panel, whereas it was absent in his mother (Figure 1).

The 88 patients analysed by the NGS panel were also investigated for whole exon deletions or duplications (exon CNVs) with DECoN, resulting in no CNV detected.

Family 5

DNA was extracted from peripheral blood of the affected proband, his parents and the healthy younger brother. Whole exome sequencing and variant filtering was performed at the Institute of Human Genetics, Technical University of Munich as described previously (Kremer et al., 2017). Briefly, exonic regions were enriched using the Agilent SureSelect Human All Exon 50 Mb V5 Kit and sequenced on an Illumina HiSeq2500 system. Reads were aligned to the UCSC reference genome hg19 with Burrows-Wheeler Aligner (version 0.7.5a). Basic sequencing statistics are reported in Supplemental Table 1. Detection of genetic variation was performed using GATK (version 3.8) and SAMtools (version 0.1.19), Pindel (version 0.2.5a7), and ExomeDepth (version 1.0.0). No known pathogenic variant or variants in known disease genes have been identified which could explain the proband's phenotype. Assuming the recessive mode of inheritance, the variants were next filtered to be rare (MAF <0.001 within ExAC and a frequency <0.05 among our internal database of 16,000 exome data sets), affect the protein sequence and potentially both alleles. This prioritization led to 10 genes with potentially bi-allelic variants. Based on the clinical and biochemical diagnosis of a mitochondrial disorder, the homozygous missense variant NM_003143.2 c.394A>G;p.Ile132Val in *SSBP1*, the only mitochondrial protein coding gene in the list, has been identified as the most promising candidate (Supplemental Table 2). Subsequent Sanger sequencing confirmed homozygous *SSBP1* variant in the proband II:2 and identified both parents and the brother (I:1, I:2 and II:4, respectively) as heterozygous carriers of the missense variant (Figure 1).

SSBP1 in silico modeling

To better understand the effects of patients' variants we analyzed their structural and functional effects using in silico methods. The VIPUR pipeline predicts the deleteriousness of protein missense variants based on energetic destabilization of the variant protein structure and inter-species conservation1. VIPUR was trained using variants with clear disruption of molecular function and provides a detailed interpretation of missense variant effects. We analyzed variants in SSBP1 using the available PDB model 3ULL (chain A). To further interpret variant effects we also collected protein functional annotations from multiple databases (UniProt, Entrez, MobiDB). As a negative control comparison we ran the same analysis for 35 variants in ExAc, presumed to be variants in random healthy individuals. The ExAc variants matched expectation with most variants obtaining neutral scores (27/35 ExAc variants were neutral). VIPUR analysis suggests that p.G40V, p.R107Q and p.E111Q have the highest disruptive potential among the identified variants (Supplemental Table 3). Functional annotations include G40 as composing part of the single strand DNA (ssDNA) binding site and this position has a high inter-species conservation score, suggesting p.G40V likely acts by destabilizing the conserved nucleic-acid interaction region. Taken all together, these structural and functional analyses suggest p.G40V disrupts SSBP1 activity by impairing its ability to properly bind and interact with ssDNA while both p.R107Q and p.E111Q prevent tetramerization (p.R107Q is predicted to prevent both dimerization and tetramerization). VIPUR predicts that p.E111Q is deleterious as E111 forms part of the SSBP1 tetramerization contacts, apparently forming a salt-bridge with H34. p.E111Q introduces a subtle change, substituting the charged side chain carboxylic acid group with a polar but uncharged amide, removing only the side chain charge while maintaining similar stereochemistry. VIPUR predicts p.R107Q is neutral although it forms part of the SSBP1

dimer interface and inspection of the protein structure suggests that R107 forms a stabilizing salt-bridge with E27, an interaction that is not currently considered by VIPUR.

mtDNA sequencing

Direct sequence analysis of the entire mtDNA molecule was performed on total DNA extracted from fibroblsts, by Next Generation Sequencing (NGS) methods (1). Fastq files were analyzed with MToolBox (2) and an in-house pipeline. Specifically, reads were aligned to the human reference genome (comprising the rCRS) using BWA (3). Aligned reads were treated for realignment with GATK (4) and for duplicate removal with PicardTools (http://picartools.sourceforge.net). Then, reads uniquely mapped to the mtDNA reference genome and with a mapping quality score ≥20 were extracted and used for variant calling with two different callers: the Unified Genotyper of GATK and the mutation-server DetermineVariants, a stand-alone of the mtDNA-server pipeline (5). In both the callers, only positions with a base quality score ≥20 were considered. Only mono-allelic sites were retained and calls were further filtered in order to avoid an excessive strand bias using a SOR (StrandOddsRatio) value ≤ 4, following the GATK Best Practice for variant filtration. Finally, a consensus of the variants called by the three callers was created and further investigated.

Fluorescence microscopy of cells

For visualization of mitochondria, the fluorescent dye MitoTracker Red-CMXRos (ThermoFisher) was added to the culture media at a final dilution of 0.1 μL/mL for 30 min. For visualization of mitochondrial nucleoids, PicoGreen dsDNA reagent (ThermoFisher) was added to the growth media at a final dilution of 3 μL/mL for 60 min. For visualization of SSBP1, after fixation and permeabilization, cells were incubated with rabbit anti-SSBP1

antibody (dilution 1:200) (6), followed by a fluorescently labeled secondary antibody (Alexa Fluor 488, ThermoFisher). Images were acquired with a confocal microscope (Leica TSC-SP8) using a 63x oil objective, high sensitivity hybrid detectors (HyDs 1 and 3) and LAS AF software. Excitation and emission wavelengths were 579 / 599 for Mitotracker red and 488 / 490-525 for Alexa Fluor 488 and PicoGreen dsDNA reagent. For mitochondrial nucleoids quantifications, ten images of each cell line were analyzed using ImageJ software, measuring the ratio between the percentage of the area occupied by nucleoids vs. the area occupied by mitochondria. For SSBP1 quantification, ten images of each cell line were analyzed using ImageJ software (NIH), measuring the corrected total cell fluorescence (CTCF) ratio between SSBP1 and MitoTracker signals.

Oxygen consumption rate

The OCR was measured as previously described (7). Oxygen concentration were measured in XFe24 Extracellular Flux Analyzer (Seahorse Bioscience), under basal condition and after injection of 10^{-6} mol/L oligomycin, 10^{-6} mol/L carbonyl cyanide 4-(trifluoromethoxy) phenylhydrazone (FCCP), 10^{-6} mol/L rotenone and 10^{-6} mol/L antimycin A. The OCR values (pmol O2/min) were normalized for protein content of each well, determined by the SRB assay.

Western Blotting

Proteins were separated on pre-cast NuPAGE 4-12% Bis-Tris Glicyne gels (Life Technologies) and then transferred on nitrocellulose membranes, using the XcellSure Lock (Life Technologies) apparatus. After blocking with 5% milk, membranes were blotted with primary antibodies specific: ACTIN (catalog ab1801), ATP5A (catalog ab14748), CS (catalog ab129095), NDUFA9 (catalog ab14713), TFAM (catalog ab47517), UQCRC2

(catalog ab14745), VDAC1 (catalog ab14734), HSP60 (catalog ab81333) and OXPHOS cocktail (catalog ab110411) were from Abcam; RNaseH1 (catalog sc-136343) was from Santa Cruz Biotechnology; POLγ (catalog D1Y6R) and TOM20 (catalog 42406) were from Cell Signaling; TWINKLE (catalog 13435-1-AP) was from Proteintech; SDHA (catalog 459200) was from Invitrogen; Tim23 (catalog 611222) was from BD; GAPDH (catalog MAB374) was from Millipore; SSBP1 (Tiranti, 1997), ETHE1 (8). Fluorescent secondary antibodies anti-rabbit or anti-mouse (Licor, catalog 926-32210 and 926-68071) were used for immunodetection using the Licor Odyssey instrument. The chemiluminescence signals of horseradish peroxidase (HRP)-conjugated secondary antibodies (Invitrogen) were revealed using Chemioluminescent HRP substrate (Millipore) and measured with Licor Odyssey instrument.

Assessment of OXPHOS complexes and respiratory supercomplexes assembly

For complexes analysis, mitoplasts were isolated from 10^6 cells/ml using 50 μg/ml digitonin and then suspended in a buffer containing $750x10^{-3}$ mol/L aminocaproic acid, $50x10^{-3}$ mol/L bis–tris, pH 7.0, and solubilized with 2.5 g of dodecyl-maltoside (DDM) for 1 g of protein. The suspension was incubated on ice for 10 min, centrifuged at 13000g and the protein content of supernatant determined. BN sample buffer (5 % Serva G Blue in $750x10^{-3}$ mol/L aminocaproic acid, $50x10^{-3}$ mol/L Bis–Tris and $0.5x10^{-3}$ mol/L EDTA) or CN sample buffer (0.1 % Red Ponceaux and 50 % glycerol) were added to mitoplast aliquots and samples were loaded on pre-cast NativePAGE Novex® Bis-Tris Gel 4-16 % gels (Life Technologies). After electrophoresis, the CN-PAGE gels were analyzed for CI IGA and CI western blotting, whereas the BN-PAGE gels were used for western blotting of the other complexes. Supercomplexes assembly study was performed as preaviously described (9) with minor modification. Briefly, mitoplasts were isolated from 10^6 cells/mL using 50 μg/ml digitonin

and protein content was determined. After centrifugation, the pellet was suspended (5 mg protein/mL) in $340x10^{-3}$ mol/L K-acetate, $70x10^{-3}$ mol/L HEPES (pH 7.4), 25% glycerol, $2.3x10^{-3}$ mol/L PMSF, and 5% (w/v) digitonin and incubated on ice for 30 min. Samples were centrifuged and the supernatant, with Supercomplexes sample buffer (5 % Serva G Blue in $750x10^{-3}$ mol/L aminocaproic acid), was loaded on pre-cast NativePAGE™ 3-12 % Bis-Tris Protein Gels (Life Technologies). Gels were analyzed for CI IGA and western blotting with antibodies against representative subunits of each complex.

Size Exclusion Chromatography

Recombinant SSBP1 proteins were applied in Size Exclusion Buffer (final: $30x10^{-3}$ mol/LHEPES-KOH pH 7.6, $250x10^{-3}$ mol/L KCl, $0.25x10^{-3}$ mol/L EDTA, $2x10^{-3}$ mol/L DTT, and 10 % glycerol) to a Superdex 200 10/300 GL column (GE Healthcare) using an AKTA FPLC system (GE Healthcare). Data were collected using UNICORN v.5.31 (GE Healthcare).

Differential Scanning Fluorimetry

Proteins at a final concentration of 1.5 mg/ml and SYPRO Orange (Molecular Probes) at a final ratio of 5X were combined in DSF Buffer (final: $30x10^{-3}$ mol/L HEPES-KOH pH 7.6, $50x10^{-3}$ mol/L KCl, $0.25x10^{-3}$ mol/L EDTA, $2x10^{-3}$ mol/L DTT, and 10 % glycerol), before transferring 20 µl of each sample to a 96-well plate in quadruplicate to account for well-to-well variability. Using a QuantStudio 7 Flex Real-Time PCR System (Applied Biosystems), the samples were heated from 25 °C to 95 °C at a ramp rate of 1.6 °C/s with detection set to the ROX reporter and with the x1-m3 filter in place. Data were collected using QuantStudio 7 Flex software (Applied Biosystems) and analyzed using Protein Thermal Shift v1.3 (Applied Biosystems). The peak of the first derivative of the thermal melting curve defines the melting

temperature (Tm) for each protein. Melting temperatures were averaged across first plate quadruplicates and then triplicate experiments before statistical analysis using GraphPad Prism software.

and then triplicate experiments before statistical analysis using GraphPad Prism software.

Functional complementation of patient-derived fibroblasts

Functional complementation of patient-derived fibroblast cell lines was done as described previously (10). In short, overexpression of SSBP1 in fibroblast cell lines was performed by lentivirus-mediated expression of the full-length SSBP1 cDNA using the ViraPower HiPerform Lentiviral TOPO Expression Kit (Thermo Fisher Scientific). SSBP1 cDNA was obtained from pDONR221 vector (GatewayDNASU Plasmid Repository, DNASU Plasmid ID: HsCD00045388). SSBP1 cDNA was cloned into the pLenti6.3/V5-TOPO expression vector and cotransfected into HEK293FT cells with the packaging plasmid mix using Lipofectamine 2000 (Thermo Fisher Scientific). After 24 h, the medium containing the DNA-Lipofectamine 2000 transfection mix was replaced with high glucose DMEM supplemented with 10% FBS. After further 72 h, the viral particle containing supernatant was collected and used for subsequent transduction of the fibroblast cell lines. Selection of stably expressing cells was performed using 5 μg/ml Blasticidin (Thermo Fisher Scientific) for 2 weeks. Stably transduced fibroblasts were kept under selection for further analysis.

Zebrafish husbandry

All embryos were obtained from natural matings of either wild type (WT; ZDR) or transgenic adults carrying a mitochondrial reporter, *Tg(XlEef1a1:mlsEGFP)* (11). Embryos were raised at 28.5 ºC in egg water (0.3 g/L NaCl, 75 mg/L CaSO4, 37.5 mg/L NaHC03, 0.003 % methylene blue) until phenotyping or tissue harvest at 2 or 4 days post fertilization (dpf). All

experiments (morpholino or CRISPR/Cas9 injection) were performed at doses in which the lethality rate of any experimental batch is not significantly different from that of control.

CRISPR/Cas9 genome editing

To disrupt the *ssbp1* locus in zebrafish we used ChopChop (12) to identify a CRISPR single guide (sg)RNA targeting exon 4. We performed *in vitro* transcription of sgRNA using the GeneArt Precision gRNA Synthesis kit (Thermo Fisher). To determine sgRNA efficiency, we injected 50 or 100 pg sgRNA plus 100 or 200 pg of Cas9 protein (PNA Bio) into the cell of single cell stage embryos (1 nl volume; 30 embryos per batch). At 2 dpf, we isolated genomic DNA from individual embryos, PCR-amplified the *ssbp1* target region, and amplification products were subjected to heteroduplex analysis (denatured and reannealed slowly: 95 ºC for 2 min, -2 ºC/s to 85º C, and then -0.1 º C/s to 25 ºC). The resulting product was migrated on a 20 % PAGE gel (Thermo Fisher) to evaluate sgRNA targeting as indicated by heteroduplexing. PCR product from single embryos was then selected for TA cloning into the TOPO4 vector (Thermo Fisher); 16 colonies from each PCR product were sequenced to estimate the percentage of mosaicism in each embryo.

Transient suppression of *ssbp1*

We designed a translation blocker morpholino (tb-MO) 5'-TGAGAAGGCTGCAATAACCCCACGC-3' targeting the start ATG in exon 2 (GeneTools LLC). We injected tb-MO at 3 different doses (1 ng, 2 ng and 3 ng; 1 nl per injection; 30 embryos/batch) into embryos at the one to four cell stage. To validate MO efficiency, we performed immunoblotting of total protein extracted from pools of embryos harvested at 2 dpf (n=25 embryos/pool). We removed the yolk from anesthetized embryos with sharp forceps, and homogenized them in RIPA buffer (50 mM HEPES [pH 7.6], 1% Triton X-100,

0.1% SDS, 50 mM NaCl, 0.5% sodium deoxycholate, 1 mM NaF, and 0.02 mM DTT). Embryos were centrifuged for 15 minutes and the supernatant was retained. We quantified protein with the BCA assay (Pierce); separated 50 μg/well using a mini-PROTEAN TGX Precast Gel (4%–15%; Bio-Rad); and transferred proteins to a polyvinylidene difluoride (PVDF) membrane. We incubated the membrane overnight in primary antibody (PBS; 3% BSA; rabbit anti-SSBP1 antibody [Proteintech, cat # 12212-1-AP; 1:1000 dilution]; and goat anti-β-actin was used as loading control [Santa Cruz Biotechnology, cat # sc-47778; Lot # 1209; 1:2000 dilution]). Secondary detection was performed with buffer containing PBS; 3% BSA, and anti-rabbit IgG-HRP conjugate (Santacruz Biotechnology cat # sc-2357; Lot # Lo209; 1:5000 dilution) or anti-goat IgG-HRP conjugate (Santacruz Biotechnology cat # sc-2922; Lot# K2202; 1:5000 dilution]. Immunoblots were developed with Super Signal West Pico PLUS chemiluminescent substrate (ThermoFisher Scientific) according to the manufacturer's instructions, and a ChemiDoc Imaging System (Bio-Rad) was used for chemiluminescence detection.

SSBP1 **plasmids, mutagenesis and** ***in vitro*** **mRNA transcription**

We obtained a full-length WT human *SSBP1* open reading frame entry clone (ENST00000265304.10; IOH3259; Thermo Fisher) and transferred it to pCS2+ destination vector using LR clonase II (Thermo Fisher) recombination. The variants identified in cases were introduced into the ORF by site directed mutagenesis, as described (13); integrity of all plasmids was confirmed by sequencing. We generated capped WT and mutant mRNA with the mMessage mMachine SP6 Transcription kit (Ambion) using the linearized pCS2+ vector as a template. We used 3 ng tb-MO and 150 pg mRNA for *in vivo* complementation experiments.

Whole mount immunostaining and microscopy

We evaluated the area of the optic nerve chiasm at 2 dpf. We dechorionated embryos manually with forceps, anesthetized them with tricaine, and fixed them overnight in Dent's solution (40 % MeOH plus 20 % DMSO) as described (14-16). We performed primary detection with anti-acetylated tubulin antibody (Sigma-Aldrich, T7451, 1:1,000 overnight at 4 ºC) and secondary detection with Alexa Fluor 488 goat anti-mouse IgG (Invitrogen; A11001, 1:1,000). We mounted all the embryos in a 3% agarose mold, and oriented them ventrally facing towards the objective of the microscope. We imaged embryos using fluorescence microscopy (AZ100, Nikon) with a 10X objective mediated by a Nikon digital sight black and white camera and NIS Elements software (Nikon). We measured the area of the optic nerve chiasm using ImageJ (NIH), by outlining the region within the notochord. Statistical comparisons were performed using a paired t-test. Experiments were performed at least three times.

Bright field microscopy and assessment of edema phenotypes

Larvae were imaged with an AZ100 microscope and Digital sight color camera facilitated with NIS Elements software using a 2x objective (all from Nikon). We performed qualitative assessment of *ssbp1* morphants at 4 dpf for edema phenotypes and categorized them as Normal, Class I (pericardial edema) or Class II (pericardial edema and periorbital or yolk sac edema).

Live imaging of *Tg(XlEef1a1:mlsEGFP)* larvae

We assessed mitochondrial (mt)DNA depletion at either 15 dpf (mutants) or 2 dpf (morphants) using a transgenic zebrafish line that expresses mitochondrially targeted GFP (EF-1α promoter driving expression of the mitochondrial localization sequence of zebrafish

COXVIII). Live embryos or larvae were oriented laterally and fluorescent signal was captured at 8X magnification with an AZ100 microscope (Nikon) with consistent exposure time. GFP intensity was quantified in the lens using ImageJ (NIH).

qRT-PCR analysis of mitochondrial markers in zebrafish

We quantified mitochondrial markers (*mt-nd1* and *mt-cox1*) from whole embryo cDNA. Total RNA was extracted from both controls and morphants at 2 dpf using Trizol (Thermo Fisher) according to manufacturer instructions. We synthesized cDNA with QuantiTect Reverse Transcription kit (QIAGEN), and performed qRT-PCR using two independent pairs of primers per gene with the SYBR green master mix and detection on an ABI7900 (Applied Biosystems). *b-actin* was used for normalization. The qPCR data were analyzed using the ΔCt method.

q-PCR analysis of mtDNA copy number in zebrafish

We quantified mtDNA copy number in zebrafish *ssbp1* morphants as described (17,18) Briefly, DNA was extracted at 2dpf from embryos pools of controls and morphants injected with 3 ng *ssbp1* tb MO, (n=30 embryos/pool). We performed q-PCR using *mt-nd1* as the mitochondrial marker and *polg1* as the reference for nuclear genomic DNA. We used the SYBR green master mix and detection on an ABI7900 (Applied Biosystems). The qPCR data were analyzed using the ΔΔCt method. Experiments were performed in triplicate wells and repeated four times.

Web resources

- *Annovar:* http://annovar.openbioinformatics.org/en/latest/
- *BWA-MEM*: https://www.ncbi.nlm.nih.gov/pubmed/19451168

- *CADD:*
- *CHOPCHOP*: http://chopchop.cbu.uib.no/
- *DECoN*: https://github.com/RahmanTeam/DECoN
- *DeNovoGear*: https://www.ncbi.nlm.nih.gov/pubmed/23975140
- *Ensembl:* http://ensembl.org/
- *ExAC/pLI*: https://www.ncbi.nlm.nih.gov/pubmed/27535533
- *Exomiser*: https://www.ncbi.nlm.nih.gov/pubmed/24162188
- *GATK*: https://www.ncbi.nlm.nih.gov/pubmed/20644199
- *gnomAD*: http://gnomad.broadinstitute.org
- *MTR*: http://mtr-viewer.mdhs.unimelb.edu.au/mtr-viewer/
- *PCAN*: https://www.ncbi.nlm.nih.gov/pubmed/27923364
- *Picard*: http://broadinstitute.github.io/picard/
- *Platypus*: https://github.com/andyrimmer/Platypus/tree/master/extensions/DeNovo
- *Polyphen2*: https://www.ncbi.nlm.nih.gov/pubmed/20354512
- *RefSeq*: (https://www.ncbi.nlm.nih.gov/refseq/)
- *Sapientia*: www.sapientia.co.uk
- *SIFT*: https://www.ncbi.nlm.nih.gov/pubmed/12824425
- *VEP*: https://www.ncbi.nlm.nih.gov/pubmed/27268795
- *Vipur*: https://github.com/EvanBaugh/VIPUR

Supplemental References

1. Caporali L, et al. Peculiar combinations of individually non-pathogenic missense mitochondrial DNA variants cause low penetrance Leber's hereditary optic neuropathy. *PLoS Genet.* 2018;14(2):e1007210.
2. Calabrese C, et al. MToolBox: a highly automated pipeline for heteroplasmy annotation and prioritization analysis of human mitochondrial variants in high-throughput sequencing. *Bioinformatics.* 2014;30(21):3115-3117.
3. Li H, Durbin R. Fast and accurate short read alignment with Burrows-Wheeler transform. *Bioinformatics.* 2009;25(14):1754-6170.
4. DePristo MA, et al. A framework for variation discovery and genotyping using nextgeneration DNA sequencing data. *Nat Genet.* 2011;43(5):491-501.
5. Weissensteiner H, et al. mtDNA-Server: next-generation sequencing data analysis of human mitochondrial DNA in the cloud. *Nucleic Acids Res*. 2016;44(W1):W64-W69.
6. Tiranti V, et al. Identification of the gene encoding the human mitochondrial RNA polymerase (h-mtRPOL) by cyberscreening of the Expressed Sequence Tags database. *Hum Mol Genet.* 1997; 6(4):615-625
7. Del Dotto V, et al. Deciphering OPA1 mutations pathogenicity by combined analysis of human, mouse and yeast cell models. *Biochim Biophys Acta Mol Basis Dis.* 2018;1864(10):3496-3514.
8. Tiranti V, et al. Ethylmalonic encephalopathy is caused by mutations in ETHE1, a gene encoding a mitochondrial matrix protein. *Am J Hum Genet.* 2004;74(2):239-252.
9. Del Dotto V, et al. OPA1 Isoforms in the Hierarchical Organization of Mitochondrial Functions. *Cell Rep.* 2017;19(12):2557-2571.
10. Kremer LS, Prokisch H. Identification of Disease-Causing Mutations by Functional Complementation of Patient-Derived Fibroblast Cell Lines. *Methods Mol Biol*. 2017; 1567:391-406

11. Kim MJ, Kang KH, Kim CH, Choi SY. Real-time imaging of mitochondria in transgenic zebrafish expressing mitochondrially targeted GFP. *Biotechniques.* 2008;45(3):331-334.
12. Montague TG, Cruz JM, Gagnon JA, Church GM, Valen E. CHOPCHOP: a CRISPR/Cas9 and TALEN web tool for genome editing. *Nucleic Acids Res.* 2014;42(Web Server issue):W401-W407.
13. Niederriter AR, Davis EE, Golzio C, Oh EC, Tsai IC, Katsanis N. In vivo modeling of the morbid human genome using Danio rerio. *J Vis Exp.* 2013;(78):e50338.
14. Borck G, et al. BRF1 mutations alter RNA polymerase III-dependent transcription and cause neurodevelopmental anomalies. *Genome Res.* 2015;25(2):155-166.
15. Guissart C, et al. Dual Molecular Effects of Dominant RORA Mutations Cause Two Variants of Syndromic Intellectual Disability with Either Autism or Cerebellar Ataxia. *Am J Hum Genet.* 2018;102(5):744-759.
16. Margolin DH, et al. Ataxia, dementia, and hypogonadotropism caused by disordered ubiquitination. *N Engl J Med.* 2013;368(21):1992-2003.
17. Artuso L, et al. Mitochondrial DNA metabolism in early development of zebrafish (Danio rerio). *Biochim Biophys Acta*. 2012;1817(7):1002-11.
18. Quiros PM, Goyal A, Jha P, Auwerx J. Analysis of mtDNA/nDNA Ratio in Mice. *Curr Protoc Mouse Biol.* 2017;7(1):47-54.